Biological efficacy of novel metal complexes of Nitazoxanide: Synthesis, characterization, anti-COVID-19, antioxidant, antibacterial and anticancer activity studies

Abeer A. Sharfalddin [a,*], Enas Inas Muta'eb Alyounis [b], Abdul-Hamid Emwas [b], Mariusz Jaremko [c,*]

[a] Department of Chemistry, Faculty of Science, King Abdulaziz University, P.O. Box 80203, Jeddah 21589, Saudi Arabia
[b] King Abdullah University of Science and Technology (KAUST), Thuwal 23955-6900, Saudi Arabia
[c] Smart-Health Initiative (SHI) and Red Sea Research Center (RSRC), Division of Biological and Environmental Sciences and Engineering (BESE), King Abdullah University of Science and Technology (KAUST), Thuwal, Jeddah, Saudi Arabia

ARTICLE INFO

ABSTRACT

It has been repeatedly reported that nitazoxanide (NTZ) exhibits a wide range of antiviral activities against various viral infections and has shown antimicrobial properties against anaerobic bacteria, helminths and protozoa. To improve these properties, three novel metal complexes were synthesized. The bidentate characteristic of the NTZ ligand was characterized by different spectroscopic techniques, including Fourier transform infrared (FT-IR), thermogravimetric, nuclear magnetic resonance (NMR) and UV − visible spectroscopy. The geometries of the formed compounds were evaluated by density functional theory, and the results revealed that NTZ-Ru(III) has an octahedral geometry, while NTZ-Au(III) and NTZ-Ag(I) complexes have distorted square planar structures. Binding between the metal complexes and calf thymus DNA (Ct-DNA) has been studied via absorption spectra. Moreover, human albumen serum (HAS) titration has been carried out to test their susceptibility to interact with a major target molecule via absorption and fluorescence spectroscopic techniques. Several in vitro bioassays were performed to evaluate the biological activity, antibacterial potency against E. coli, antioxidant activity and cytotoxicity of the ligand and the obtained complexes. The results showed that complexes Ru(III) and Au(III) have the highest radical scavenging percentage while the Ag(I) demonstrated the greatest antibacterial activity. Moreover, the metal complexes presented potentially effective against E. coli. Furthermore, compared with NTZ-Ag and the free ligand, the in vitro cytotoxicity assay showed that both NTZ-Ru(III) and NTZ-Au(III) exhibited significant anticancer activity against HeLa cells. The efficiency of the novel compounds as antivirals was tested by molecular docking with two COVID-19 receptors to obtain all interaction details.

© 2022 The Author(s). Published by Elsevier B.V. This is an open access article under the CC BY-NC-ND license (http://creativecommons.org/licenses/by-nc-nd/4.0/).

1. Introduction

Nitazoxanide was used long ago as an antiprotozoal [1], antibacterial [2], antiviral [3] and anticancer agent against various human cancer cell lines [4]. Nitazoxanide (NTZ), presented in Fig. 1, is known as 2-(acetyloxy)-N-(5-nitro-2-thiazolyl) benzamide and was discovered by Jean Francois Rossignol [5]. Its effectiveness against both bacterial infections and parasites led to its approval in the United States (Alinia®, Romark Laboratories) for diarrhea treatment caused by Giardia intestinalis and C. parvum (July 2004) [6]. Interestingly, the presence of thiazolyl in its structure yielded immunomodulating properties that are useful for the treat-

ment of broad-spectrum viruses, such as chronic hepatitis C (HCV) and acute uncomplicated influenza [7]. Moreover, it has demonstrated in vitro efficacy against rotavirus, norovirus, hepatitis B virus (HBV) and hepatitis C virus (HCV) [8]. Many reports have presented the inhibition potency of nitazoxanide against several human cancer cell lines and tumor models both in silico and in vitro [9]. This due to the unique structure has two moieties in one molecule, which are the nitrothiazole moiety and salicylamide moiety (Fig. 1), attributed to multiple activities. The nitrothiazole part exhibits a practical inhibition of protozoal, antiproliferative and anti-infective effects [10]. Additionally, it is a good antioxidant that could disrupt pyruvate: ferredoxin oxidoreductase by interfering with the necessary electron transfer for anaerobic protozoa in the bacteria and for their energy metabolism [11]. Although the other moiety, salicylamide, plays the same role as an antioxidant,

---

* Corresponding authors.
E-mail address: sharfalddin.aa@gmail.com (A.A. Sharfalddin).

A.A. Sharfalddin, E. Inas Muta'eb Alyounis, A.-H. Emwas et al.

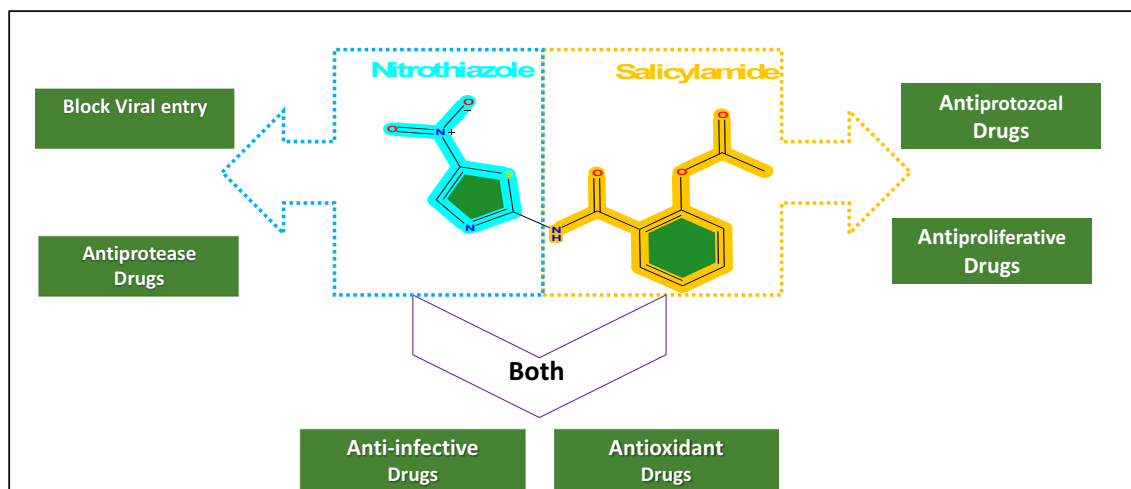*Journal of Molecular Liquids 368 (2022) 120808*

Fig. 1. The chemical structure of NTZ and some features of the two moieties.

anti-infective and analgesic, the role of blocking viral entry and host cell membrane fusion and regulating immune responses characterize the structural features of the nitrothiazole (salicylamide) part [8].

Introducing metal ions into bioactive molecules increases their pharmacological abilities and properties [12]. According to Tweed's chelation theory, metal ions could increase the lipophilicity of the organic drug by donating electrons from their orbitals to the metal and reducing the polarizability around the metal and then delocalizing electrons over the metal complexes [13]. Moreover, metal ions decrease the drug molecules toxicity and enhance compound stability in biological systems. Excitingly, its reported that metal complexes exhibited antiviral properties against some known viruses, such as influenza and SARS viruses [14]. This potency starts at the beginning of the infection process by blocking the entry of the virus into the host cells and to the stage of the virus budding progressions via the RNA replication process [14].

In this work, three metal ions, Ru(III), Au(III) and Ag(I), reacted with NTZ to obtain stable metal complexes. We characterized these compounds *via* Fourier transform infrared (FT-IR), thermogravimetric (TG), NMR and UV − visible spectroscopy. Moreover, the chemical parameters and chemical reactivity of the synthesized compound were estimated using a density functional theory (DFT) approach. The bioactivities of the new complexes, such as antioxidant, antibacterial, anticancer and antiviral activities, were evaluated using different bioassay approaches, including *in vitro* methods. The study started with testing the binding susceptibility toward small biological molecules such as DNA helix and human serum albumin (HSA). The antibacterial activity was evaluated against negative microorganisms (*Escherichia coli*), whereas the cytotoxicity test was performed in two human cancer cell lines (MCF-7 and HELA) and normal cells. Moreover, molecular docking, a theoretical technique, was used to examine the molecular interactions of the newly synthesized compounds and assess their hypothetical inhibitory capacity toward SARS-CoV-2.

2. Materials and methods

2.1. Chemicals and instruments

Nitazoxanide with 99 % purity (NTZ) and the metal salts of RuCl$_3$·3H$_2$O, KAuCl$_4$ and AgNO$_2$ were purchased from Sigma Aldrich and used without further purification. Human serum albumin (HSA, A1887; globulin and fatty acid free) and calf thymus

DNA (Ct-DNA) were used for the biological study and purchased from Sigma Aldrich.

Infrared spectra (IR) for the ligand and metal complexes were recorded on a Bruker infrared spectrophotometer in the range of 400–4000 cm^{-1}. The molar conductance of the 10^{-3} M complex solution in DMF was measured on a HACH conductivity meter. A Bruker 600 MHz spectrometer was used to record the ^{1}H NMR spectra in DMSO d$_6$ solution. Electronic spectra of the metal complexes were obtained with a Shimadzu UV/Vis spectrometer in the range of 200–800, while fluorescence experiments were carried out on a Cary Eclipse spectrofluorometer from 300 to 600 nm. Thermogravimetric analysis TG-DTG experiments were conducted using a NETZSCH STA 449F1 thermal analysis system under air at a flow rate of 30 mL/min and a 10 °C/min heating rate for the temperature range of 25–800 °C, and the data were analyzed by Proteus software. The percentage of the metal ions was calculated thermogravimetrically as metal oxides.

2.2. Synthesis procedure

Ruthenium(III) chloride trihydrate salt was dissolved in ethanol and activated by the reflexing method until the black color turned green [15], while 1 mM Au(III) and Ag(I) salts were dissolved in ethanol before being added to the free ligand. A freshly prepared nitazoxanide (NTZ) solution in ethanol and DMSO with a ratio of 70–30 % was added dropwise to the previous metal solution with continuous stirring. Then, the reaction mixtures were run in the reflexing system for 5 h. The colored precipitates were collected by filtering and washed with cold ethanol. The complexes were kept in a desiccator.

[Ru(NTZ)$_2$Cl$_2$]Cl: color: Dark brown. IR (FT-IR, cm^{-1}): - (NH), 1750 (C=O), 1664 (C=O), 1600 (N—C), 1384, 1292 (NO$_2$), 1170 (C—O), 874, 651. ^{1}H NMR (DMSO d$_6$, 500 MHz, ppm): 12.40 (b, 1H, NH), 8.70 (s, 1H, thiazole), 7.82 (dd, 1H, CHAr), 7.70 (td, 1H, CHAr), 7.47 (td, 1H, CHAr), 7.32 (dd, 1H, CHAr), 2.24 (s, 3H, CH$_3$). UV-Vis: (DMSO, 10^{-3}, nm): 269, 379 s 434, 500. Molar conductance. (10^{-3} M, DMSO, Ω^{-1} cm^2 mol^{-1}): 90.40.

[Au(NTZ)$_2$]Cl$_3$: color: Bluish-green. IR (FT-IR, cm^{-1}): 3359 (NH), 1755 (C=O), 1664 (C=O), 1522 (N—C), 1384, 1292 (NO$_2$), 1153 (C—O), 870, 650. ^{1}H NMR (DMSO d$_6$, 500 MHz, ppm): 13.60 (s, 1H, NH), 8.70 (s, 1H, thiazole), 7.82 (dd, 1H, CHAr), 7.70 (td, 1H, CHAr), 7.47 (td, 1H, CHAr), 7.32 (dd, 1H, CHAr), 2.24 (s, 3H, CH$_3$). UV-Vis: (DMSO, 10^{-3}, nm): 268, 321 s. Molar conductance. (10^{-3} M, DMSO, Ω^{-1} cm^2 mol^{-1}): 225.

A.A. Sharfalddin, E. Inas Muta'eb Alyounis, A.-H. Emwas et al.

Journal of Molecular Liquids 368 (2022) 120808

[Ag(NTZ)$_2$]NO$_3$: color: wheat. IR (FT-IR, cm^{-1}): 3430 (NH), 1760 (C=O), 1669 (NH-C=O), 1520 (N—C), 1384, 1292 (NO$_2$), 1177 (C—O), 874, 651. UV-Vis: (DMSO, 10^{-3}, nm): 281, 376 s. Molar conductance. (10^{-3} M, DMSO, Ω^{-1} cm^2 mol^{-1}): 61.10.

2.3. Computational calculations

The optimization of the obtained novel metal complexes was carried out by a *Gaussian 09* [16] to account the most stable electronic structures of all compounds using the density function theory (DFT) method. The hybrid functional-based DFT method known as B3LYP was used with the basis set of the triple-zeta 6–311+G(d, p) basis sets for the free ligand, while the correlation-consistent basis set (LANL2DZ) was employed for Ru(III), Au(III) and Ag(I) metal ions [17]. The output files were visualized by *Gauss View* software and showed the optimized geometries did not have an imaginary frequency, which confirmed that the structures were on the potential energy surface. Moreover, the HOMO and LUMO energies and orbital levels were extracted using *Gauss View* to calculate the following essential quantum parameters: energy gap ($E_{gap} = E_{LUMO} - E_{HOMO}$), absolute electronegativities ($\chi = -E_{HOMO} + E_{LUMO}/2$), absolute hardness ($\eta = E_{LUMO} - E_{HOMO}/2$), chemical potentials ($\mu = -\chi$), global softness ($S = 1/2\eta$), and global electrophilicity ($\omega = \mu^2/\eta$)[18].

2.4. In vitro binding of the complexes to Ct-DNA

A spectroscopic approach was carried out to study the ability of the metal complexes to bind to Ct-DNA. The experiments employed a constant compound concentration and gradually increasing (1.57–5.15 μM) of Ct-DNA concentrations. The Ct-DNA was dissolved in a buffer solution (pH 7.4) and confirmed to be free of protein using the UV absorbance ratio (A$_{260}$/A$_{280}$), which was in the range 1.8–1.9 [18,19]. The effective binding constants (K$_b$) were evaluated using the Benesi-Hildebrand equation

$$\frac{A_o}{A - A_o} = \frac{\varepsilon G}{\varepsilon G^- G - \varepsilon G} + \frac{\varepsilon G}{\varepsilon H^- G - \varepsilon G} \times \frac{1}{K[DNA]}$$

where A_0 and A are the absorbances of the complex and complex with DNA, respectively, and εG and $\varepsilon H^- G$ are the absorption coefficients of the complex and the complex-DNA, respectively. The K$_b$ was determined as the intercept to slope ratios from the graphic representation of $A_o/(A - A_o)$ vs 1/[DNA].

2.5. In vitro binding of the complexes to HSA

Two standard techniques were employed to analyze the HSA binding experiments. Spectroscopic and emission spectroscopy titration experiments were performed between the constant concentration of HSA and the tested samples. First, the HSA solution concentration was determined by the absorption spectra obtained at 278 nm and extinction coefficient 35,219 M^{-1}cm^{-1} using quartz cuvettes of 1 cm path length. The absorption spectral method and the binding constant calculations were explained in our previous work [20]. Regarding the fluorescence technique, free HSA was excited at 280 nm, and the emission wavelengths were set at 300–400 nm. The increasing concentrations of the metal complex were added to a constant concentration of HSA, and the fluorescence emission was measured. We used the Stern–Volmer equation to calculate the K$_{SV}$, F$_o$/F (or I$_0$/I) = 1 + KSV [HSA], where F$_o$ is the fluorescence intensity in the absence of a quencher and F is the fluorescence intensity in the presence of metal complexes. K$_{SV}$ is the Stern–Volmer quenching constant obtained from the slope of the plot of F$_o$/F [Complex] [18,21].

2.6. Molecular docking platforms

Assessing the potency of the free NTZ and the metal complexes as antiviral agents was performed with the computational molecular docking software Molecular Operating Environment (MOE) against the crystal structure of SARS-CoV-2 protease (PDB ID: 6LU7) and SARS-CoV-2 spike glycoprotein (PDB ID: 6VXX). The SARS-CoV-2 S glycoprotein is present on the surface of the virus and facilitates entry into the host cell membrane, which is the first target that could be addressed. The viral replication and transcription processes are mediated by SARS-CoV-2 M^{pro}, which has a significant pocket similar to that of all coronaviruses, making it another target in our study. All PDF files were obtained from the RCSB Protein Data Bank (PDB). The proteins were prepared by deleting the repeated chains, water molecules and co-ligands and then correcting the protonation and distribution of partial charges via the MOE-Quick prep feature. The active sites were located with the MOE-Site finder tool and expressed as dummy atoms by the application. The protein SARS-CoV-2 spike glycoprotein (PDB ID: 6VXX) has 1273 amino acids, and we chose the S1 subunit (14–685) as a binding pocket in charge of receptor binding during viral infection [22]. The optimized geometries for the metal complex files were converted to MDB files and saved as a database. The docking protocol was carried out under the default option, which has the following parameters: triangle matcher method for placing the compound, GBVI/WSA dG for rescoring and London dG for scoring. The results are presented as 5 posies with the related binding energy (S kcal/mol). The first poise has been chosen for analysis in the next stage.

2.7. Estimation of biological activity

2.7.1. In vitro antibacterial activity

The antibacterial activities of all synthesized compounds were evaluated against pathogenic strains by applying the agar disc diffusion and broth dilution methods [23]. The bacterial pathogen used in this study was *Escherichia coli* (ATCC: 25922), which is a gram-negative bacterium. The bacterial strain was cultured onto a Muller–Hinton agar (MHA) plate and incubated for 18–24 h at 35 °C. All the examined compounds were prepared by dissolving 20 mg of each compound in 1 mL of DMSO. Thus, DMSO was used as a negative control for all the samples examined and Ampicillin was used as a standard drug. A bacterial culture (which was adjusted to McFarland 0.5 standard solution (1.5x 108 CFU/mL)) was used to lawn Hinton agar plates using a sterile swab. Paper discs with a 5-mm diameter were impregnated individually with a constant amount (100 μg/mL) of the compounds. The antibacterial activity of each test sample was determined by measuring the diameter of the zone of inhibition and comparing it with that of the standard drug. The Ampicillin was also evaluated using the minimal inhibitory concentration (MIC) method. The test assay was assessed twice and no inhibition zone was found for the DMSO sample.

2.7.2. Cytotoxicity assessment (MTT assay)

The vitality of the cultured cells was investigated using enzymatic reduction of the tetrazolium dye MTT to formazan. To evaluate anticancer activity, three cell lines were used, including two tumor cell lines (MCF-7: a human breast cancer cell line, and HELA: cancerous cervical tumor cells) and a normal cell line (HEK293: human embryonic kidney cells). The three cell lines were grown in Dulbecco's modified Eagle's medium (DMEM) supplemented with 0.2 % sodium bicarbonate and 10 % fetal bovine serum (FBS). The cells were maintained in a 5 % CO$_2$−95 % atmosphere under high humidity at 37 °C. Cells were assessed for cell viability by the trypan blue dye exclusion assay as described earlier [24].

Batches of cells showing more than 98 % cell viability were used in this study, where cell viability was assessed using the MTT assay as described previously [25]. Briefly, 10,000 cells were plated in 96-well culture plates and allowed to adhere for 24 h in a CO_2 incubator at 37 °C. After the exposure, MTT (5 mg/ml of stock PBS) was added (10 μl/well of 100 μl of cell suspension) to each well, and the plates were incubated further for 4 h in a CO_2 incubator. Then, the supernatant was discarded, and 200 μl of DMSO was added to each well and mixed gently. The developed color was read at 550 nm in an Evolution 201 reader (Thermo Scientific, Waltham, MA, USA). Untreated control sets were also run under identical conditions. All the values were corrected from background absorbance.

The survivability percentage x100% was calculated using (ODt/ODc), where ODc denotes the density of untreated cells and ODt signifies the density of wells treated with the test compound. By graphing the association between the number of cells that survived and the quantities of compounds, survival curves for each cancer cell line and the normal cell line following treatment with the specified substance were constructed. Using concentration chart pad Prism software, the 50 % inhibitory concentration (IC_{50}) was determined from charts of the dose response curve for all (San Diego, CA, USA).

2.7.3. Assay to assess antioxidant properties

The ABTS*+ radical-scavenging activity of the synthesized complexes was determined according to Re et al. [26]. 2,2′-Azinobis-[3-ethylbenzothiazoline-6-sulfonic acid] (ABTS) was dissolved in twice-distilled water to yield a 7 mM solution. The ABTS radical cation solution was prepared by allowing the ABTS solution to react with the $K_2S_2O_8$ solution (final concentration: 2.45 mM) for 12–16 h in the dark at room temperature. To determine the antioxidant capacity of the synthesized complexes and the standard or reference (ascorbic acid in this case), the ABTS solution was diluted with an appropriate solvent (methanol) to an absorbance of 0.7 ± 0.01. Ten microliters of standard or samples was added to 190 μl of ABTS reagent in a 96-well plate. The plate was shaken for 10 s at medium speed, followed by 5 min of incubation in the dark, and the absorbance was measured at 734 nm. Both the samples and ascorbic acid were used at different concentrations (1, 3, 5, and 10 μg/ml). All measurements were carried out at least three times. The percent inhibition of absorbance at 734 nm was calculated using the formula.

ABTS·+ scavenging effect (%) = ((AB–AA)/AB) × 100,

where AB is the absorbance of ABTS radical + methanol and AA is the absorbance of ABTS radical + sample synthesized complex/or the standard.

3. Results and discussion

3.1. Characterizing the structure of the formed metal complexes.

The spectroscopic titration of the metal ion solution and the free ligand showed an inflection at approximately 0.33, indicating that the molar ratio of the metal to the ligand was 1:2 (M:L). **Figure S1** and this ratio were used to prepare the correct stoichiometric equivalents of the reactants. The obtained compound structures were confirmed by NMR, IR, and UV–Vis spectroscopy, as well as conductance measurements (Table 1). The formed complexes are stable in air and soluble in DMSO and DMF. Moreover, the formation stability constant for the complexes was calculated using Equation [27] and arranged according to the stability in descending order of NTZ-Ru(IIII) > NTZ–Au(III) > NTZ–Ag(I) (34.37 × 10^5, 17.92 × 10^5, and 4.22 × 10^5, respectively) which showed ruthenium (III) practical formation stability, followed by gold (III). The

conductance of the three complexes was greater than 50 Ω^{-1} cm^2 mol^{-1}, indicating the electrolytic nature of the metal complexes [28]. In detail, the Ru(III) complex showed two types of ions in the solution, indicating that one Cl ion is outside the coordination sphere. However, Au(III) showed a higher conductance value and revealed that Cl ions do not participate in the coordination geometry. Similarly, the conductance value of Ag(I) suggested the presence of one NO_3 ion outside the sphere.

The IR spectra were recorded for the free ligand and the metal complexes in the range of 4000–400 cm^{-1} to investigate the binding coordination mode for metal complexes. The NTZ ligand has six donating sites that can coordinate with transition metals, which give the molecule extraordinary properties. They are an amide group, two carbonyl oxygens, a nitrogen atom in thiazole and an ester oxygen. A careful comparison between the NTZ spectrum and the metal complex spectra presented in Fig. 2 and Table 1 showed that the stretching band for υNH vanished upon coordination to Ru(III), while Au(III) and Ag(I) compound's band shifted to higher frequencies. This result indicates the association of NH is the main binding site in the Ru(III) complex and it does not associate in the other complexes. Additional evidence for this notion is the finding results of ester stretching at 1770 cm^{-1} and 1160 cm^{-1} that was allocated to C=O and C—O, respectively. Although the carbonyl group showed a shift to a low range, it was still maintained in all metal complexes, which eliminates the involvement of the coordination sphere. However, the band located at 1160 cm^{-1} in the free ligand shifted to a higher frequency and had a low intensity for only Ru(III) due to the binding effect to the ester oxygen. The frequency mode for amide C=O and C=N in the thiazole ring showed a redshift and an intensity reduction, respectively, upon chelation to Au(III) and Ag(I) ions, which suggested that binding at these sites occurred in the organic molecule.

For a deeper investigation, the ^1H NMR spectra of Au(III) and Ru(III) were compared with the NTZ spectrum and are illustrated in Fig. 3.

The free NTZ spectrum presents six signals corresponding to CH-Ar in the benzyne ring (7.85, 7.47, 7.70 and 7.32 ppm), CH_3 (2.24 ppm) and NH (13.60).

The singlet signal at 13.60 ppm corresponding to the amine –NH group in NTZ shifted to a low range in the Ru(III) complex and it was maintained in the Au(III) spectrum. This excludes the binding of Au(III) to NH and confirms the coordination in the Ru(III) compound.

3.2. Thermogravimetric analysis

The change in mass upon increasing the temperature is a practical approach to confirm the coordination structure, stability of the formed complex and number of lattice water molecules [18]. TG/DTG curves for the three metal complexes were obtained in the temperature range of 25–800 °C. The first decomposition for the Ag(I) compound started at 25–180 °C through the loss of one lattice water and NO_3 from the sphere. The complete decomposition started with a sharp and strong DTG curve at 219 °C with a weight loss of 65.3 % in the second step, **Figure S2**.
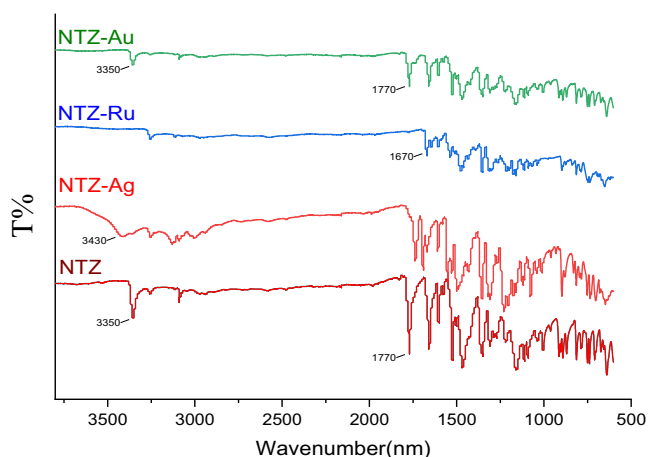
The thermogram of the Au(III) compound does not show an inflection below 144 °C, which could indicate the presence of 2Cl (7.1 %) without hydrated water and solvent. This was followed by the final step starting from 320 to 795 °C and mass loss of 68.7, **Figure S2**.

The ruthenium (III) curve in **Figure S2** demonstrates two decomposition steps at 279 for the first stage, with a mass loss of 10.6 %, corresponding to two Cl molecules and one water molecule, which were similar to the theoretical value (10.5 %). The pyrolyzis of the rest of the ligand part was in the second stage, corresponding

Table 1
The analytical and physical properties, IR assignments and electronic transition assignments of the free NTZ and metal complexes.

| Compound	M.W. (g/mol)	Color	Λm (Ω^{-1} cm^2 mol^{-1})	Electronic Spectra		IR spectral bands (ν, cm^{-1})				
				λ^{max} (nm)	Assign	υ (NH)	υ (C=O)	υ (NH-C=O)	C—O	C=N
NTZ	307	yellow	3	260	n → π	3350	1770	1660	1160	1600
				347	π → π*					
[Ru(NTZ)₂Cl₂]Cl	820	Dark brown	90.40	269	n → π	–	1740	1670	1170	1600
				379	π → π*					
				434	ML-CT					
				500	d-d					
[Au(NTZ)₂] Cl₃	916	Bluish green	225	268	n → π	3350	1770	1664	1163	1520
				321	π → π*					
[Ag(NTZ)₂NO₃]	767	wheat	61.10	281	n → π	3430	1767	1669	1177	1522
				376	π → π*					

Fig. 2. Comparative representations of the FT-IR spectra of the free ligand and metal complexes.

to a 52.8 % mass loss. The final weight losses the metal complexes were attributed to both metal oxide residues and carbon. All thermal mass loss and decomposition stages are listed in **Table S2**, which were in agreement with the speculated formulas for the coordinated compounds.

3.3. Computational calculations

Theoretical calculations using DFT method and 6-31G, LANL2DZ basis sets for NTZ ligand and metal complexes, respectively, were used to confirm the best structure formation and to predict their activities. We built the ligand input file according to the crystal structure of NTZ [29]. The output was extracted and visualized by *Gauss View*, which provided an illustration of the structure with atomic numbering and labeling as shown in Fig. 4. Initially, the charge distribution on the ligand molecule is used to distinguish the donor sites, which practically affect the molecular coordination system [30].

The calculated natural atomic charge (NBO) values for the ligand are ranked in the following order: C—O > NH > O=C-NH > C=O > C=N (thiazole), with values of 0.64, 0.61, 0.60, 0.54 and 0.52, respectively.
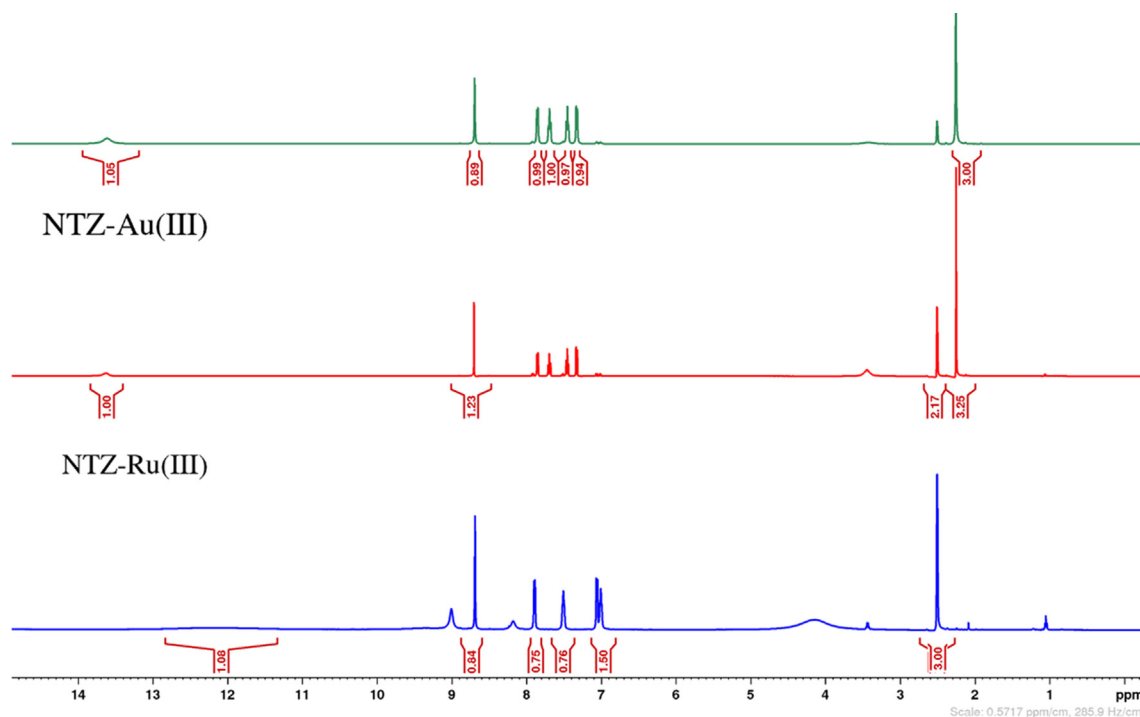
Fig. 3. The ¹H NMR spectra of NTZ and the Ru(III) and Au(III) complexes.
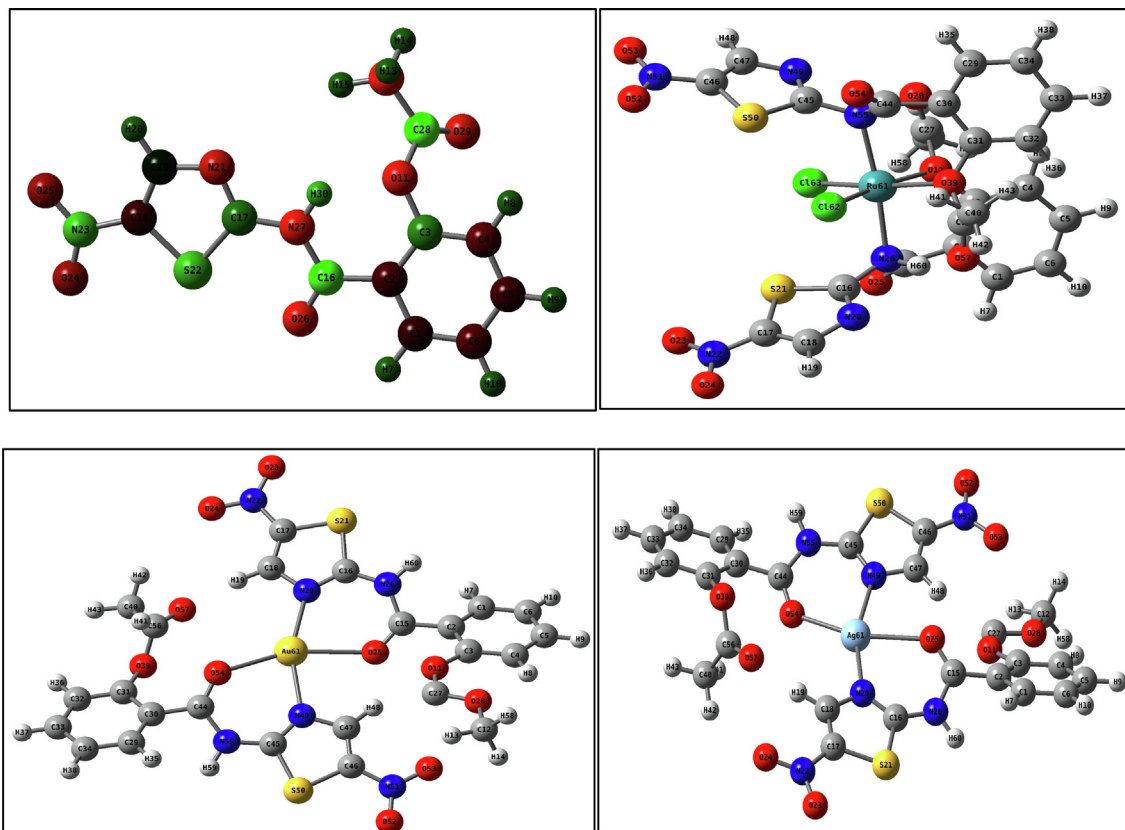
Fig. 4. Optimized structures with atom numbering and labels indicating the color charge distribution for the NTZ ligand using DFT/B3LYP (red color shows negative charge, and green color shows positive charge).

The spectroscopic analysis of the Ru(III) complex suggested that the structure was formed by bidentate ligands via amine and ester oxygen (they have the highest negative charges in the molecule). In contrast, Au(III) and Ag(I) were coordinated to the amide oxygen and the nitrogen in the thiazole ring. The optimized geometries for the ligand and metal complexes are presented in Fig. 4.

Moreover, we compared the extracted calculated FT-IR spectra for the compound with the solid sample spectra in the range 500–3800 cm^{-1}, and we found a strong and reliable correlation between them, which provides another perspective on the suggested structures. Additionally, the formed bonds between the metal ion and nitrogen and oxygen atoms were in the range of 2.10–2.66 Å, which revealed the small and medium ionic characteristics of these bonds[20a]. The bond angles showed that the Ru(III) complex adapted a distorted octahedral geometry, while Au(III) and Ag(I) have a distorted square planar.

Another feature of the DFT calculation is the prediction of the biological potency of the metal complexes [28] using essential activity parameters that were calculated from the highest occupied molecular orbital energy (E_{HOMO}) and the lowest unoccupied molecular orbital energy (E_{LUMO}), which are illustrated in Fig. 5. The molecular orbital HOMO for the Ru(III) complex was distributed among the thiazole and nitro groups, whereas these groups in one ligand had the highest electron orbitals in both gold and silver complexes. Otherwise, the LUMO orbitals were centered around the Ru(III) ion and spread over the Au(III) compound molecule. The LUMO in the Ag(I) complex was distributed mainly over one of the ligand molecules. This is a practical indicator that metal ion centers can react as accepters to react with biological residues. The energy values for both HOMO and LUMO for the metal complexes are extracted to calculate the difference between the orbital energies that contribute to the energy gap, E_g. This is another activ-ity metric of the metal complex and is shown with the essential quantum parameters (electrophilicity (ω), global hardness (η), chemical potential (μ), absolute softness (σ), electronegativity (χ) and global softness (S)) in **Table S3**. Generally, the energy gap, E_g, was reduced after coordination of the ligand to the investigated metal ions that smooth electronic transitions and increase the reactivity and softness of the compound. Electrophilicity (ω) is a description of the molecule's ability to capture electrons from the surrounding environment. Therefore, we can arrange the complexes according to this feature as follows: Ru(III) > Au(III) > Ag(I) > NTZ.

3.4. Estimating the binding capability of drugs to biological molecules.

Scientists usually investigate the pharmacological potency of new drugs by testing their susceptibility to interactions with a major target (DNA molecules or proteins) as part of the development strategy of drugs designed. Therefore, two approaches were used to explore the interaction between metal complexes and DNA or protein in this study.

3.4.1. DNA binding studies.
3.4.1.1. Spectrophotometric titration. DNA is a small biomolecule target, and any modification of its structure due to binding to a specific compound can be measured by diverse methods, such as spectroscopy, fluorescence, viscosity measurements and circular dichroism studies [31]. Among these techniques, spectroscopic titration is the easiest and least expensive method [28]. UV–Vis spectroscopic analysis was performed in the range of 200–800 nm by adding DNA gradually to the metal complex solution.

The change maxima absorption bands for the fixed-concentration solution in buffer for NTZ metal compounds are pre-
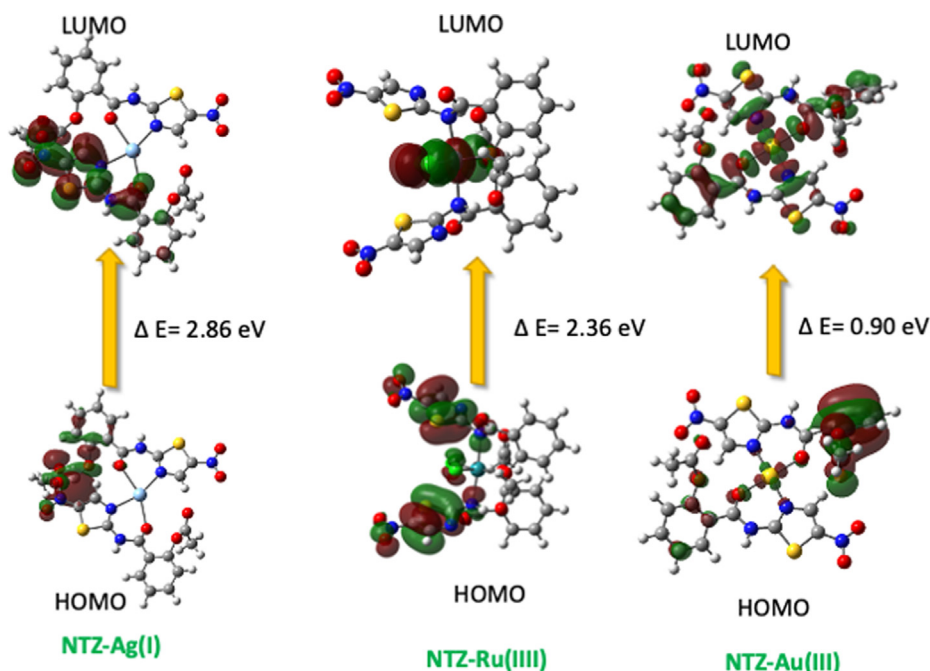
A.A. Sharfalddin, E. Inas Muta'eb Alyounis, A.-H. Emwas et al.

Journal of Molecular Liquids 368 (2022) 120808

Fig. 5. HOMO and LUMO charge densities of the studied complexes according to the B3LYP/LAND level.

sented in **Figures S3**. The NTZ-Ru(III) spectrum showed a blueshift with great chromism change. Moreover, the hypochromic molar absorptivity of this spectrum indicated a strong change in DNA structure due to damage to the DNA double-helical conformation. However, both the NTZ-Au(III) and Ag(I) complex maxima peaks shifted slightly to higher frequencies, which revealed binding to DNA. In the case of NTZ-Ag(I), it presented a hypochromic effect after the interaction with the DNA molecules and suggested inter-calative binding. Otherwise, the hyperchromic effect of NTZ-Au(III) and the redshift resulted from denaturation of the DNA helix and led to a weakness of the hydrogen bond between the paired bases in the DNA double helix. The existence of single-stranded DNA and different bases in free form in the tested solution resulted in an increase in the absorbance [31]. Accordingly, this result suggests an electrostatic interaction between the positive charge in the metal complex and the negative phosphate group [32]. The intrinsic binding constants (K_b) with the binding parameters are shown in **Table S4**. The calculated values showed that NTZ-Au(IIII) has the highest binding value.

3.4.2. HSA binding studies.

3.4.2.1. Spectrophotometric titration.

The free HSA λ^{max} at 278 nm moved slightly to 1–3 nm upon gradual addition of the metal complex to a constant concentration of HSA. This was associated with a sharp increase in the absorption intensity in Fig. 6. **Figure S4** (hy-perchromic mode) indicated strong binding of all the investigated metal complexes through hydrogen bonds. Predominantly, electrostatic interactions could result from morphological changes in the secondary structure of HSA [33]. The arrangement of the investigated complexes in ascending order according to the intrinsic binding constant (K_b) is as follows: 1.45×10^4, 3.67×10^4 and 1.49×10^5 for NTZ-Ag(I) < NTZ-Ru(III) < NTZ-Au(III), respectively. The gold compound also showed strong binding to HSA as well as to Ct-DNA, while Ru(III) ranked second.

3.4.2.2. Fluorescence titration study.

Human albumin serum has a fluorescence excitation at 295 nm due to the amino acid residue tryptophan (Trp) located in subdomain IIA of the HSA structure

[34] and a clear emission ae 350 nm. The quenching of the fluorescence intensity of HSA presented in Fig. 7 and **Figure S5** resulted from the interaction of the indole moiety of the Trp chromophore with metal complexes, which reduced the emission quantum yield. There was a negligible change in the wavelength of the emission maximum of HSA, just 2–3 nm, assuming there was small modification of the cavity polarity around the Trp residue [35]. The slope of the plot of F_o/F_{vs} and [metal complex] that was utilized to calculate the fluorescence constant (K_{vs}) was 7×10^6, 4×10^6 and 3×10^6 M^{-1} for NTZ-Au(III), NTZ-Ru(III) and NTZ-Ag(III), respectively.

3.5. Biological activity

3.5.1. In silico assay through MOE docking.

Currently, a molecular docking procedure is used to predict the biological efficiency of the molecules and estimate the preferred ligand orientation when it binds to the site pocket on the targeted protein [22]. Initially, all metal complexes exhibited better binding affinities to both proteinases than the free NTZ. Regarding binding properties against the SARS-CoV-2 glycoprotein (6VXX), NTZ-Ag(I) ranked highly with −8.695 kcal/mol, followed by the NTZ-Au(III) complex, as presented in Table 2. Among the three interaction types, the ionic interaction of NH in the Au(III) molecule with the ASP287 amino acid had a bond strength of −4.4 kcal/mol. Interestingly, we also docked the investigated compounds against 6VXX on the S2 subunit pocket (686–1273), which is responsible for cell membrane fusion [22] and the results showed that NTZ-Ag(I) is more effective among the tested complexes. In this practical interaction, shown in Table 3, Ag(I) metal binding to the ASP 867 amino residue was observed, along with hydrophobic pi-H binding between NH in the ligand moiety and HIS 1058.

Compared with SARS-CoV-2 (6LU7), the obtained results are shown in descending order: NTZ-Au(III) > NTZ-Ag(I) > NTZ-Ru(III) > NTZ, with practical binding of NTZ-Au(III). Amino acid ASN142 has played a different binding role in NAT-Au(III), which once interacted with the hydrophobic pi-H H-donor, while the last two were set with accepted hydrogen molecules donated from
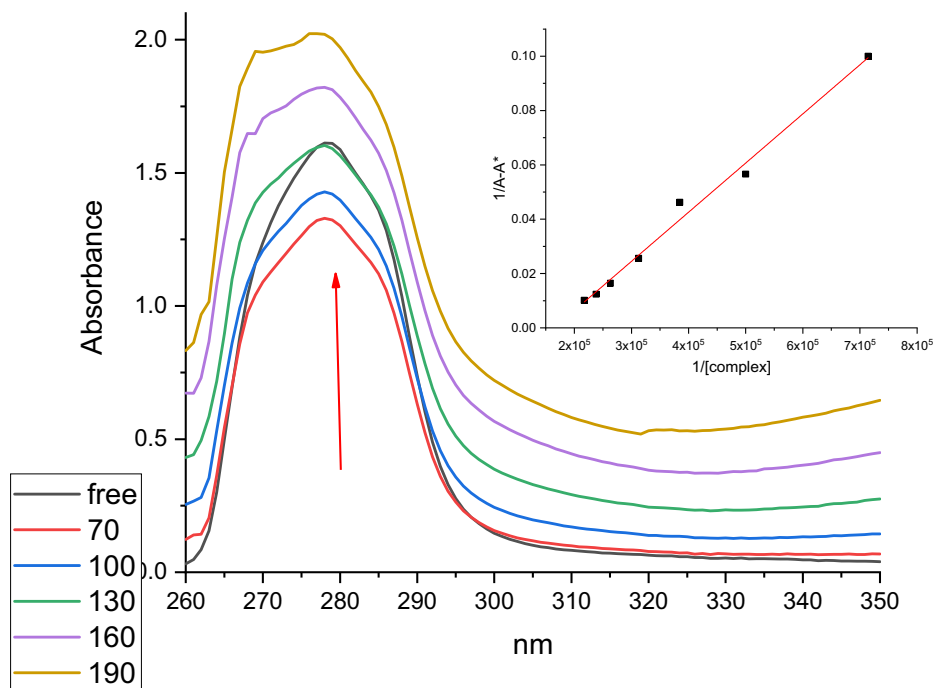
Fig. 6. Absorption spectra of HSA in the absence and presence of increasing amounts of NTZ-Au(III) complex. The change in the absorbance is indicated by the arrow.
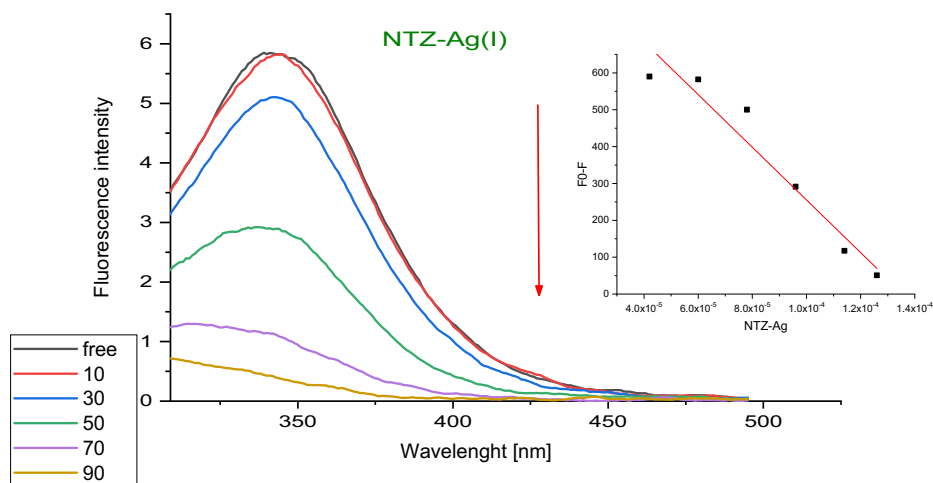

Fig. 7. Emission spectrum of HSA in the presence and absence of the NTZ-Ag(I) complex. The inset shows the plots of the emission intensity of F0/F vs [NTZ-Ag] to determine the K_{SV}.

Table 2
Binding score (kcal mol^{-1}) for NTZ and its metal complexes toward SARS-CoV-2 protein receptors.

	Binding affinity for SARS-CoV-2 (6VXX)		Binding affinity for SARS-CoV-2 (6LU7)
	S2 subunit	S1 subunit	
Free NTZ	−6.08996	−5.24522	−6.39776
NTZ-Ru(III)	−6.30576	−5.57292	−6.58961
NTZ-Ag(I)	−8.17329	−8.69500	−7.27620
NTZ-Au(III)	−7.40361	−7.8977	−7.40030

HIS163 and GLN189 (Table 3). Moreover, the effect of the thiazole ring is clear based on the interaction of the sulfur atom with ASN 142, which blocks viral entry.

As shown in Table 2, among the high-ranked complexes, both NAT-Au(III) and NAT-Ag(I) were effective against both the SARS-CoV-2 protease and SARS-CoV-2 glycoprotein.

The binding properties and ranking of the repurposed complexes against the 6VXX and 6LU7 proteins are shown in **Tables S5 and S6**.

3.5.2. Antioxidant assay

There are different methods to test the antioxidant properties of the investigated compound, such as the SOD, ABTS$^{•+}$ and DPPH assays [36]. The ABTS assay is based on the reduction of blue/green ABTS·+ by antioxidants, which is convenient and the most popular application. The results of the ABTS·+ method were determined by measuring the absorption reductions at 734 nm after the interaction with free NTZ or its complexes. Ascorbic acid was used as a reference standard to compare the antioxidant activity of the com-

Table 3
The binding of Ag(I) and Au(III) complexes as the highest binding score with the SARS-CoV-2 proteins.

protein	2D snapshot
SARS-CoV-2 glycoprotein (S1 subunit)	
SARS-CoV-2 glycoprotein (S2 subunit)	
SARS-CoV-2 (6LU7)	
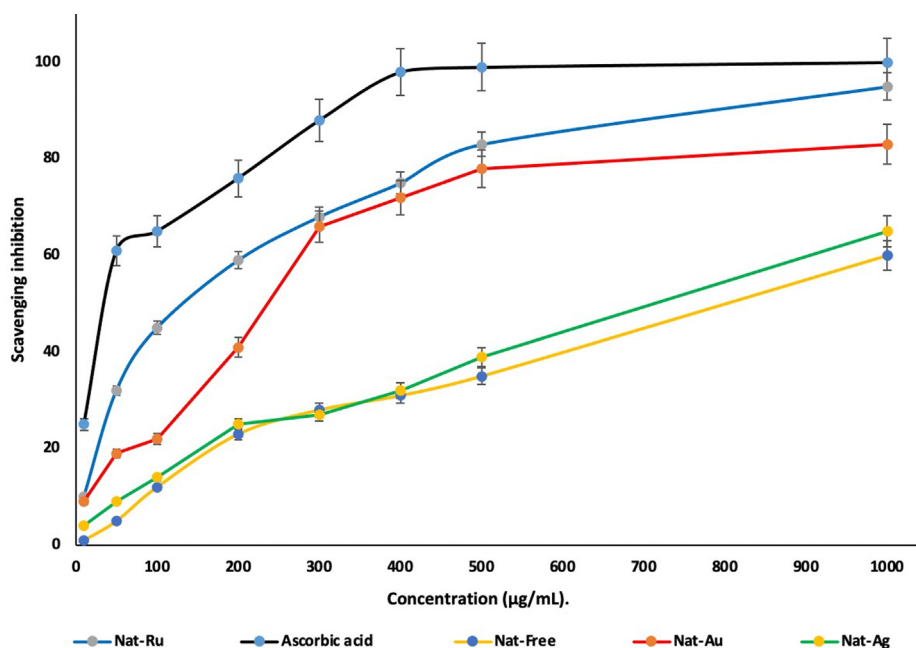
Fig. 8. Scavenging properties of ligand and its metal complexes (% inhibition vs different concentrations (μg/mL). Ascorbic acid used as a standard. Data are means ± SD, n = 3.

A.A. Sharfalddin, E. Inas Muta'eb Alyounis, A.-H. Emwas et al.

Journal of Molecular Liquids 368 (2022) 120808

pounds. The calculated results are presented according to scavenging activity (%) as follows: 58, 91, 64 and 80 % for free NTZ, NTZ-Ru(III), NTZ-Ag(I) and NTZ-Au(III), respectively. Compared with ascorbic acid, all metal complexes demonstrated moderate to good antioxidant activity. The complex of Ru(III) and Au(III) had the strongest radical scavenging percentage (Fig. 8).
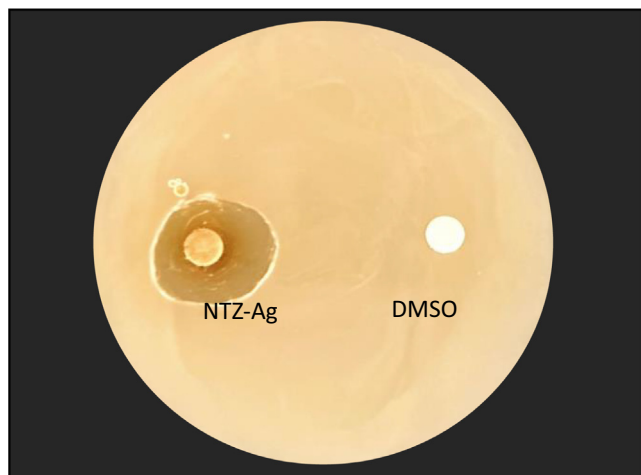
3.5.3. Antibacterial activity

Gram-negative bacteria (*Escherichia coli*) have been used for many studies as an antibacterial model [37]. It was shown that it causes foodborne diseases, which are one of the most threatening public health problems worldwide [43]. The in vitro antibacterial activities of the ligand and the metal complexes were investigated using this bacterium by applying disc diffusion and the MIC method and were compared with those of a standard drug (ampicillin). The diameter of growth inhibition is shown in Table 4 with the minimum inhibitory concentration (MIC). In general, the metal complexes displayed better inhibitory effects than the NTZ ligand

against the tested bacterial strain, with zone inhibition in the range of 12–28 mm. Among all of the metal complexes, the compound NTZ-Ag showed the highest antibacterial activities, with a zone inhibition diameter of 28 mm against the Gram-negative bacterial strain for E. coli (Fig. 9). The remaining complex inhibition zones on the agar plate are shown in **Figure S6**.

Generally, the MIC of these complexes was better than that of the free ligand. The MIC results for the metal complexes showed that NTZ-Ag inhibited bacterial growth at 5.5 µM, which was very close to the result of the standard drug (ampicillin), 3.5 µM. Comparing the inhibition growth of free AgNO₃ salt and the obtained NTZ-Ag compound toward *Escherichia coli*, the reported concentration 6.5 µM is practical value for more than 24 h and upper than 8.5 µM of AgNO₃ can shows complete inhibition [38]. Otherwise, NTZ-Ag shows better minimum inhibition concentration (5.5 µM) after just 24 h. The practical antibacterial of the metal complexes was attributed to the enhancement of the metal ions by increasing their lipophilicity to penetrate the cell, thus inhibiting the growth of the microbes according to Overtone's and Tweedy's concept [32].

Table 4
Antimicrobial activity associated with the free ligand and metal complexes presented according to the diameters (mm) of inhibition zones, activity index % and minimum inhibitory concentration (MIC/µM).

Compound	Inhibition zones (mm)	Activity index (%)	Minimum Inhibition concentration (MIC, µM)
Free NTZ	8	24	105
NTZ-Ru(III)	20	61	7.5
NTZ-Ag(I)	28	85	5.5
NTZ-Au(III)	12	37	27.5
Ampicillin	33	100	3.5

3.5.4. Cytotoxicity assessment (MTT assay)

The cytotoxicities of the three synthesized complexes and the free ligand were assessed by the MTT assay. Notably, NTZ was originally developed as an antimicrobial medicine, but it has also been found to have anticancer properties. NTZ's anticancer activity has been confirmed in numerous human cancer cell lines and tumor models [4b,39].

The following cell lines are the most common types of carcinomas: MCF-7, a human breast cancer cell line; HELA, cancerous cervical tumor cells; and HEK293, human embryonic kidney cells [21]. The cytotoxic activities against the three cell lines were determined according to the dose values of potential drug exposure required to reduce survival in the cell lines to 50 % (IC₅₀) and are presented in Table 5 and compared with cisplatin as a standard reference [20a].

Both NTZ-Ru(III) and NTZ-Au(III) showed significant anticancer activity against HELA cells compared with NTZ-Ag(I) and the free ligand. Moderate cytotoxic activity was revealed when MCF7 cells were treated with the NTZ-Au(III) complex, while the ruthenium compound showed the most potent cytotoxic action against MCF-7 cells, with an IC₅₀ value = 10.5 µg/mL. Moreover, they demonstrated practical and very strong inhibition against the HELA cell line even compared with the standard reference, cisplatin, with values of 6.5 and 8.9 µg/mL for NTZ-Ru(III) and NTZ-Au(III), respectively.

The micromolar concentration (µM) values were well correlated with the µg/mL results. Interestingly, the obtained compounds showed high selectivity when there was no cytotoxicity toward the normal cell line (HEK cells). The free ligand showed moderate cytotoxicity to the tumor cell lines, which is in accordance with previous studies [4b,39].

Fig. 9. Antibacterial activity of the NTZ-Ag complex with gram-negative bacteria (Escherichia coli). DMSO was used as a negative control.

Table 5
Cytotoxic activity measurement based on the MTT assay of the ligand and its metal complexes against three human cell lines (MCF-7: a human breast cancer cell line, HELA: cancerous cervical tumor cells, HEK293: human embryonic kidney cells). Data are the means ± SD, n = 3.

compound	MCF-7		HELA		HEK293
	µg/mL	µM	µg/mL	µM	µg/mL
NTZ-free	62 ± 4	202	78 ± 10	254	1050 ± 10
NTZ -Ru(III)	10.5 ± 2	12.8	6.5 ± 3	7.9	265 ± 5
NTZ -Ag(I)	39 ± 4	50.8	45 ± 2	58.7	660 ± 3
NTZ -Au(III)	25 ± 5	27.3	8.9 ± 4	9.7	675 ± 5
Cisplatin	2.43 [22]		17.2 [45]		–

IC₅₀ (µg/mL): 1–10 (very strong), 11–20 (strong), 21–50 (moderate), 51–100 (weak) and greater than 100 (noncytotoxic).

A.A. Sharfalddin, E. Inas Muta'eb Alyounis, A.-H. Emwas et al.

Journal of Molecular Liquids 368 (2022) 120808

4. Conclusion

Herein, we report newly synthesized metal complexes with NTZ ligand to enhance their bioactivities. The new compounds were characterized based on ^{1}H NMR, IR, UV–Vis, TGA, conductance measurements and molar ratios to determine their chemical structure and formulae. Spectrometric titration was used to examine the interaction of complexes with DNA and HSA. The gold complex showed the best binding ability to both tested biological molecules. The geometry of the molecules was optimized using a computational approach to assert the modification of the compound's bonds and angles after coordination to metal ions. Furthermore, the NTZ-Ag complex showed a high binding energy toward the SARS-CoV-2 glycoprotein (6VXX), which showed its ability to block viral entry. The docking data showed that both NTZ-Ag and NTZ-Au are good inhibitors of the SARS-CoV-2 (6LU7) protein. In addition, we showed that they also have antibacterial properties and are promising antioxidant reagents. We conclude that adding metals to this ligand enhanced the adsorption of the complex on cell membranes, resulting in increased penetration, easier DNA base binding, and efficient cell killing activities.

Data Availability Statement: All relevant data are within the manuscript and its Supplementary Materials.

CRediT authorship contribution statement

Abeer A. Sharfalddin: Conceptualization, Methodology, Software, Writing – original draft. **Enas Inas Muta'eb Alyounis:** Investigation, Writing – original draft. **Abdul-Hamid Emwas:** Writing – review & editing. **Mariusz Jaremko:** Writing – review & editing.

Data availability

Data will be made available on request.

Declaration of Competing Interest

The authors declare that they have no known competing financial interests or personal relationships that could have appeared to influence the work reported in this paper.

Acknowledgement

Appendix A. Supplementary data

Supplementary data to this article can be found online at https://doi.org/10.1016/j.molliq.2022.120808.

References

[1] A.C. White Jr, Expert review of anti-infective therapy 2 (2004) 43–49.
[2] V.R. Anderson, M.P. Curran, Drugs 67 (2007) 1947–1967.
[3] J.–F. Rossignol, Antiviral research 110 (2014) 94–103.
[4] a) H. Fan-Minogue, S. Bodapati, D. Solow-Cordero, A. Fan, R. Paulmurugan, T.F. Massoud, D.W. Felsher, S.S. Gambhir, Molecular cancer therapeutics 12 (2013) 1896–1905;
b) N. Di Santo, J. Ehrisman, Mutation Research/Fundamental and Molecular Mechanisms of Mutagenesis 768 (2014) 16–21.
[5] C.M. Theodos, J.K. Griffiths, J. D'onfro, A. Fairfield, S. Tzipori, Antimicrobial agents and chemotherapy 42 (1998) 1959–1965.
[6] B. Amadi, M. Mwiya, J. Musuku, A. Watuka, S. Sianongo, A. Ayoub, P. Kelly, The Lancet 360 (2002) 1375–1380.
[7] M. Elazar, M. Liu, S.A. McKenna, P. Liu, E.A. Gehrig, J.D. Puglisi, J.F. Rossignol, J.S. Glenn, Gastroenterology 137 (2009) 1827–1835.
[8] A.S. Lokhande, P.V. Devarajan, European Journal of Pharmacology 891 (2021).
[9] a) D. F. Alonso and H. G. Farina, *International Journal of Antimicrobial Agents* **2020**, *56*, 106125; b) U. Arshad, H. Pertinez, H. Box, L. Tatham, R. K. Rajoli, P. Curley, M. Neary, J. Sharp, N. J. Liptrott and A. Valentijn, *medRxiv* **2020**.
[10] B. Colín-Lozano, I. León-Rivera, M.J. Chan-Bacab, B.O. Ortega-Morales, R. Moo-Puc, V. López-Guerrero, E. Hernández-Núñez, R. Argüello-Garcia, T. Scior, E. Barbosa-Cabrera, Bioorganic & Medicinal Chemistry Letters 27 (2017) 3490–3494.
[11] A. Hemphill, J. Mueller, M. Esposito, Expert opinion on pharmacotherapy 7 (2006) 953–964.
[12] A.A. Sharfalddin, M.A. Hussien, Journal of Molecular Structure (2020).
[13] B. Tweedy, Phytopathology 55 (1964) 910–914.
[14] M. Pal, D. Musib, M. Roy, New Journal of Chemistry 45 (2021) 1924–1933.
[15] H. Sahyon, A. El-Bindary, A. Shoair, A. Abdellatif, Journal of Molecular Liquids 255 (2018) 122–134.
[16] M. Frisch, G. Trucks, H. B. Schlegel, G. E. Scuseria, M. A. Robb, J. R. Cheeseman, G. Scalmani, V. Barone, B. Mennucci and G. Petersson, *Inc., Wallingford CT* **2009**, *201*.
[17] P.J. Hay, W.R. Wadt, The Journal of chemical physics 82 (1985) 299–310.
[18] A.A. Sharfalddin, A.-H. Emwas, M. Jaremko, M.A. Hussien, PloS one 16 (2021) e0256186.
[19] H.B. Howsaui, A.A. Sharfalddin, M.H. Abdellattif, A.S. Basaleh, M.A. Hussien, Applied Sciences 11 (2021) 9067.
[20] a) A.A. Sharfalddin, A.H. Emwas, M. Jaremko, M.A. Hussien, New Journal of Chemistry (2021);
b) S. Al-Harthi, J.I. Lachowicz, M.E. Nowakowski, M. Jaremko, Ł. Jaremko, Journal of inorganic biochemistry 198 (2019).
[21] A.S. Basaleh, F.Y. Alomari, A.A. Sharfalddin, N.S. Al-Radadi, D. Domyati, M.A. Hussien, Molecules 27 (2022) 2796.
[22] K.F. Adebambo, N. Haji, Computational Molecular Bioscience 11 (2021) 19–49.
[23] a) X. Wang, X. Xie, Y. Cai, X. Yang, J. Li, Y. Li, W. Chen, M. He, Molecules 21 (2016) 340;
b) N.S. Gwaram, H.M. Ali, H. Khaledi, M.A. Abdulla, A.H.A. Hadi, T.K. Lin, C.L. Ching, C.L. Ooi, Molecules 17 (2012) 5952–5971.
[24] M. Siddiqui, G. Singh, M. Kashyap, V. Khanna, S. Yadav, D. Chandra, A. Pant, Toxicology in Vitro 22 (2008) 1681–1688.
[25] a) B. A. Moosa, S. Sagar, S. Li, L. Esau, M. Kaur and N. M. Khashab, *Bioorganic & Medicinal Chemistry Letters* **2016**, *26*, 1629-1632; b) A. Hussain, M. Alajmi, M. T. Rehman, S. Amir, F. Husain, A. Alsalme, M. Siddiqui, A. AlKhedhairy and R. Khan in *Copper (II) complexes as potential anticancer and Nonsteroidal anti-inflammatory agents, Vol.* vitro, **2019**.
[26] R. Re, N. Pellegrini, Free Radical Biol. Med 26 (1999) 1231.
[27] A.A. Sharfalddin, M.A. Hussien, Journal of Molecular Structure 1228 (2021).
[28] A.A. Sharfalddin, A.-H.-M. Emwas, M. Jaremko, M.A. Abdulala, Frontiers in Chemistry 9 (2021).
[29] F.P. Bruno, M.R. Caira, G.A. Monti, D.E. Kassuha, N.R. Sperandeo, Journal of Molecular Structure 984 (2010) 51–57.
[30] A. Sharfalddin, B. Davaasuren, A.-H. Emwas, M. Jaremko, Ł. Jaremko, M. Hussien, PloS one 15 (2020) e0239200.
[31] M. Sirajuddin, S. Ali, A. Badshah, Journal of Photochemistry and Photobiology B: Biology 124 (2013) 1–19.
[32] A.M. Abu-Dief, N.M. El-Metwaly, S.O. Alzahrani, A.M. Bawazeer, S. Shaaban, M. S.S. Adam, Journal of Molecular Liquids 322 (2021).
[33] S. Tabassum, M. Zaki, M. Ahmad, M. Afzal, S. Srivastav, S. Srikrishna, F. Arjmand, European Journal of Medicinal Chemistry 83 (2014) 141–154.
[34] O. A. Chaves, A. P. d. O. Amorim, L. H. Castro, C. M. R. Sant'Anna, M. C. De Oliveira, D. Cesarin-Sobrinho, J. C. Netto-Ferreira and A. B. Ferreira, *Molecules* **2015**, *20*, 19526-19539.
[35] J. Tian, X. Liu, Y. Zhao, S. Zhao, Luminescence: The journal of biological and chemical luminescence 22 (2007) 446–454.
[36] a) O.A. El-Gammal, A.A. El-Bindary, F.S. Mohamed, G.N. Rezk, M.A. El-Bindary, Journal of Molecular Liquids 346 (2022);
b) A. Floegel, D.-O. Kim, S.-J. Chung, S.I. Koo, O.K. Chun, Journal of food composition and analysis 24 (2011) 1043–1048.
[37] a) I. Al-Younis, A. Wong, C. Gehring, FEBS letters 589 (2015) 3848–3852;
b) I. Al-Younis, B. Moosa, M. Kwiatkowski, K. Jaworski, A. Wong, C. Gehring, Frontiers in plant science (2021) 1709.
[38] C. Saulou-Berion, I. Gonzalez, B. Enjalbert, J.-N. Audinot, I. Fourquaux, F. Jamme, M. Cocaign-Bousquet, M. Mercier-Bonin, L. Girbal, PloS one 10 (2015) e0145748.
[39] D.E. Feldman, V. Chauhan, A.C. Koong, Molecular Cancer Research 3 (2005) 597–605.